The Astrophysical Journal Supplement Series, 190:322–333, 2010 October doi:10.1088/0067-0049/190/2/322

R-MATRIX ELECTRON-IMPACT EXCITATION OF Fe^{13+} AND ITS APPLICATION TO THE SOFT X-RAY AND EXTREME-ULTRAVIOLET SPECTROSCOPY OF CORONA-LIKE PLASMAS

G. Y. Liang[1], N. R. Badnell[1], J. R. Crespo López-Urrutia[2], T. M. Baumann[2], G. Del Zanna[3], P. J. Storey[4], H. Tawara[2,5], and J. Ullrich[2]
[1] Department of Physics, University of Strathclyde, Glasgow G4 0NG, UK; guiyun.liang@strath.ac.uk
[2] Max-Planck-Institut für Kernphysik, Saupfercheckweg 1, 69117 Heidelberg, Germany
[3] DAMTP, Centre for Mathematical Sciences, Wilberforce Road, Cambridge CB3 0WA, UK
[4] Department of Physics and Astronomy, University College London, London WC1E 6BT, UK
[5] National Institute for Fusion Science, Toki 509-5292, Japan
Received 2010 May 6; accepted 2010 August 16; published 2010 September 23

ABSTRACT

Accurate excitation parameters are required to interpret the ultraviolet and X-ray spectra of Fe^{13+}. In this work, we use the AUTOSTRUCTURE code to describe the atomic structure of Fe^{13+}. The 197 lowest-lying fine-structure levels of the $3s^x 3p^y 3d^z$ ($x + y + z = 3$), $3s^2 4l$, and $3s3p4\{s, p, \text{and } d\}$ configurations are included along with further correlation configurations: $3s3p4f$, $3p^x 3d^y 4l$ ($x + y = 2$), $3l4l'4l''$, and $3l3l'5l''$. The resultant level energies, lifetimes of excited states, and oscillator strengths of transitions between these levels are assessed by comparison with available experimental data and previous calculations. Electron-impact excitation data among these lowest-lying levels are generated using the intermediate-coupling frame transformation *R*-matrix method. We assess the present results by comparisons with laboratory measurement for the excitation to the metastable level $3s^2 3p^2 P^o_{3/2}$ and with available close-coupling calculations for other excitations. Using these data and a collisional-radiative model, we have analyzed soft X-ray and extreme-ultraviolet spectra from space satellite observations of a stellar corona and of solar flares, as well as measurements from an electron beam ion trap. We assess the contribution from Fe^{13+} emission lines in the solar and Procyon corona observations, and find and identify new lines in the X-ray region observed in the solar and Procyon coronae. The laboratory measurements also confirm that weak lines (218.177 Å and 224.354 Å) of Fe^{13+} contribute to the observed intensities in solar observations. The polarization effect due to the directional monoenergetic distribution of the electron energy has been taken into account in comparison with the laboratory measurements. Electron density diagnostics for the astrophysical plasma sources have been performed using the updated data so as to investigate their sensitivity to the atomic data source.

Key words: atomic data – line: identification – methods: analytical – methods: laboratory – stars: coronae – X-rays: stars

Online-only material: color figures, machine-readable table

1. INTRODUCTION

In addition to the familiar coronal green line at 5303 Å due to the $3s^2 3p^2 P^o_{3/2} \rightarrow 3s^2 3p^2 P^o_{1/2}$ transition, spectral lines of Fe^{13+} are seen in the soft X-ray and extreme-ultraviolet (EUV) spectrum of the solar corona (Acton et al. 1985; Thomas & Neupert 1994; Brown et al. 2008, hereafter BFS08). In the cool solar corona and in active regions, the green line intensity has recently been used to create isointensity contours of coronal structures (Wang et al. 1997), while EUV line intensities show strong dependence on the electron density in coronal plasmas. With a combination of high-resolution and high-quality spectra observed by present-day satellites, e.g., the EUV Imaging Spectrometer (EIS) on board *Hinode*, covering a wavelength range of 171–211 and 245–291 Å, one can map the electron density across a solar active region, as recently reported by Young et al. (2009) using EUV line pairs of Fe^{11+} and Fe^{12+}.

To date, many studies have been made of solar EUV spectra that include emission lines of Fe XIV. Brickhouse et al. (1995) reported line emissivities for Fe IX–Fe XXIV and found large discrepancies when compared with observations from the Solar EUV Rocket Telescope and Spectrograph (SERTS; Thomas & Neupert 1994), e.g., the intensity ratio, $\lambda 270.51/\lambda 257.38$, differs by a factor of two. Using the CHIANTI v1.0 database, Young et al. (1998) also noticed several large differences, e.g., for the $\lambda 274.21/\lambda 211.32$ ratio, between theory (0.35) and observation (SERTS-89: 1.01 ± 0.18). Brickhouse et al. (1995) found that the intensities of $3s3p^{24}P \rightarrow 3s^2 3p^2 P^o$ transitions relative to other Fe XIV lines are significantly higher (by up to a factor of three) than the observed. Young et al. (1998) suggested that any problem with the $3s3p^{24}P \rightarrow 3s^2 3p^2 P^o$ transitions could be due to difficulties of the atomic physics calculations for Fe^{13+}, but not due to the inaccuracies in SERTS calibration. Recently, electron beam ion trap (EBIT) measurements in the wavelength range of 107–353 Å have been performed by Liang et al. (2009a, 2009b). Moreover, a detailed comparison between the measurements, astrophysical observations, and theoretical predictions based upon the Flexible Atomic Code (FAC; Gu 2008) has been made, including emission from Fe XIV. Discrepancies between the measurements in the EBIT plasmas and astrophysical observations in Fe XIV were attributed to non-thermal electron energy distributions.

Accurate electron excitation data are known to be very important for spectroscopic modeling of the electron collision-dominated coronal-like plasmas. Mason (1994) presented a review of earlier calculations for the electron-impact excitation of Fe IX–Fe XIV, critically assessed them, and made a few recommendations for improvement in future work. Thus, following the earlier *R*-matrix work of Dufton & Kingston (1991), Storey et al. (1996, 2000) performed a larger scale 18-term (40-level)

R-matrix calculation using the JAJOM method and extended their calculation up to the electron energies of 100 Ryd. They showed that most of the discrepancies between theory and observation reported by earlier workers were resolved by their calculations. Recently, an absolute measurement by Hossain et al. (2007) of electron-impact excitation cross sections close to threshold for the dipole-forbidden $3s^23p^2\,P^o_{3/2} \rightarrow 3s^23p^2\,P^o_{1/2}$ transition demonstrated that the results of Storey et al. (2000) overestimated the broad near-threshold resonance feature by a factor of three. Modeling of those lines which have upper levels populated predominantly from the metastable $3s^23p^2\,P^o_{3/2}$ state will be affected by the uncertainty in the excitation data for this transition, although the effect of the near-threshold resonance on the excitation rate to this level is only 30% at the temperature of maximum abundance of Fe^{13+} in the solar corona. Recently, Tayal (2008) reported a 135-level Breit–Pauli *R*-matrix calculation which showed an improvement over the calculation of Storey et al. (2000) when compared with the laboratory measurement but is still 50% larger than the measured resonance peak. As a result, Tayal (2008) finds a thermally averaged collision strength for the $3s^23p^2\,P^o_{3/2} \rightarrow 3s^23p^2\,P^o_{1/2}$ transition which is 20% smaller than that reported by Storey et al. (1996) at 2×10^6 K, the temperature of maximum abundance of Fe^{13+} in the solar corona. In addition, a high-accuracy measurement of the lifetime of the metastable state has been made ($16.726^{+0.020}_{-0.010}$ ms) at the Heidelberg EBIT (Brenner et al. 2007). The incorporation of these new data into the collisional-radiative (CR) model may resolve some of the remaining discrepancies between theory and astrophysical observations. Some soft X-ray emissions originating from $n = 4$ levels of Fe^{13+} have also been detected in solar flare observations (Acton et al. 1985). However, to date, no *R*-matrix excitation data to levels of $n = 4$ are available in the literature, although these levels were included in the calculation of Tayal (2008). Indeed, to the best of our knowledge, there is not a single detailed analysis for the soft X-ray emission lines of Fe^{13+} in any previous work.

In this paper, we report on a detailed calculation of the electron-impact excitation of Fe^{13+} via the intermediate-coupling frame transformation (ICFT) method. Results for atomic structure and scattering data are presented in Section 2, and an assessment of the accuracy of these new calculations is made by comparing the results with available experimental data and the outcome of previous calculations. A brief description of the CR model is given in Section 3. In Section 4, we analyze the EUV and soft X-ray spectra from coronal-like plasmas using our new data; we also give a short description of the EUV spectroscopic experimental results obtained in an EBIT. Our work is a part of the ongoing collaborative work—the UK Atomic Processes for Astrophysical Plasmas (APAP) network,[6] a broadening of scope of the original UK RmaX network.

2. ATOMIC STRUCTURE AND COLLISION CALCULATIONS

The present close-coupling expansion includes the 197 lowest-lying levels of the (16) configurations: $[1s^22s^22p^6]3s^x\,3p^y3d^z$ ($x + y + z = 3$), $3s^24l$ ($l \in s, p, d$, and f), and $3s3p4\{s, p, d\}$. A further (77) configurations, $3s3p4f$, $3p^24l$, $3p3d4l$, $3d^24l$, $3l4l'4l''$, and $3l3l'5l''$ ($l'' \in s, p, d, f$, and g), were included so as to provide an accurate configuration interaction (CI) target expansion.

[6] http://www.apap-network.org

2.1. Level Energies

The target wavefunctions ($1s$–$4f$) were obtained from AUTOSTRUCTURE (AS; Badnell 1986) using the Thomas–Fermi–Dirac–Amaldi model potential. The relativistic effects were included perturbatively from the one-body Breit–Pauli operator (viz. mass–velocity, spin–orbit, and Darwin) without any valence electron two-body fine-structure operators. This is consistent with the operators included in the standard Breit–Pauli *R*-matrix suite of codes. The potential radial scaling parameters, λ_{nl} ($n = 1, 2, 3$, and 4; $l \in s, p, d$, and f), were obtained by a two-step optimization procedure, together with $\lambda_{5l} = -1.0$, where the negative scaling parameter signifies a hydrogenic orbital with nuclear charge number $26|\lambda|$ used to provide short-range correlation. In the first step, the average energy of the six spin-doublet terms of the $3s^23l$ and $3s3p^2$ configurations was minimized by allowing the λ_{1s}, λ_{2l}, and λ_{3l} scaling parameters to vary. Then the average energy of the four spin-doublet terms of the $3s^24l$ configurations was minimized by varying the λ_{4l} scaling parameters. This optimization procedure was determined to be the most accurate after examining a number of alternative strategies. The final scaling parameters are $\lambda_{1s} = 1.40406$, $\lambda_{2s} = 1.11073$, $\lambda_{2p} = 1.05171$, $\lambda_{3s} = 1.09423$, $\lambda_{3p} = 1.06214$, $\lambda_{3d} = 1.03547$, $\lambda_{4s} = 1.49121$, $\lambda_{4p} = 1.21552$, $\lambda_{4d} = 1.20130$, and $\lambda_{4f} = 1.39818$.

The resulting level energies are compared in Table 1[7] with experimentally derived data from NIST[8] and with previous calculations (see also Figure 1). When compared with the results of Tayal (2008) based upon the multiconfiguration Hartree–Fock (MCHF) method (Froese Fischer 1991), good agreement is noted for almost all of the excited levels, except for the first level, namely $3s^23p^2\,P^o_{3/2}$. We also performed a fully relativistic calculation using the FAC (Gu 2008), and the results show good agreement with the present AS ones and Tayal's data. The comparison with experimentally derived data (NIST compilation) shows the differences with the present AS calculation to be less than 1% for most of the excited levels, except for a few with difference up to 1.4%.

2.2. Oscillator Strengths and Lifetimes

A further test of our structure calculations is the comparison of the symmetric oscillator strengths ($gf_{i,j}$ for a given $i \longleftarrow j$ transition) with those of other calculations. Table 2 lists such a comparison for the transitions into the five lowest-lying levels. It is noted that about 96% of transitions are in agreement to within 20% with the data of Storey et al. (2000). The data of Froese Fischer et al. (2006) show excellent agreement with that of Tayal (2008). The same method (MCHF) was adopted by both, but different CIs were included in each case. When compared with the data from MCHF (Tayal 2008; Froese Fischer et al. 2006), the present AS calculations also show good agreement (within 20%) for 87% of transitions analyzed. On the other hand, we also notice that some weak transitions (e.g., $gf < 10^{-3}$) generally display larger discrepancies.

For some excited levels, reasonably accurate experimental lifetimes are available, so we make a comparison with experimental data to assess the accuracy of the present AS calculation. For the upper level ($3s^23p^2\,P^o_{3/2}$) of the coronal green line at 5303 Å, the first reported lifetime (17.52 ± 0.29 ms by Moehs

[7] Only the 10 lowest-lying levels are listed due to space. A complete list is available electronically in the online journal.

[8] http://physics.nist.gov/PhysRefData/ASD/index.html

Table 1
Level Energies (Ryd) of Fe^{13+} from Different Calculations Along with Available Experimentally Derived Data taken from NIST v3 (see footnote 8)

ID	Level Specification	NIST	AS	FAC	SMY00	Tayal08	FTI06
1	$3s^2 3p^2\ P^o_{1/2}$		0.000000				
2	$3s^2 3p^2\ P^o_{3/2}$	0.171797	0.171731	0.170682	0.168500	0.162390	0.171011
3	$3s 3p^{24}\ P_{1/2}$	2.051390	2.029851	2.030717	2.027290	2.035070	2.036023
4	$3s 3p^{24}\ P_{3/2}$	2.121330	2.099640	2.100671	2.095680	2.089440	2.107195
5	$3s 3p^{24}\ P_{5/2}$	2.208790	2.188227	2.187773	2.182290	2.180050	2.193264
6	$3s 3p^{22}\ D_{3/2}$	2.726890	2.726588	2.727226	2.730820	2.728690	2.725400
7	$3s 3p^{22}\ D_{5/2}$	2.747190	2.746476	2.746771	2.749890	2.733630	2.744937
8	$3s 3p^{22}\ S_{1/2}$	3.323330	3.349164	3.357370	3.362570	3.327640	3.336307
9	$3s 3p^{22}\ P_{1/2}$	3.540360	3.574638	3.583459	3.583710	3.538640	3.567765
10	$3s 3p^{22}\ P_{3/2}$	3.613280	3.650423	3.658998	3.657130	3.646450	3.644856

Notes. The explanation of the column labels is the same as for the caption of Figure 1. ID represents the level ordering in the present AS calculation.
(This table is available in its entirety in a machine-readable form in the online journal. A portion is shown here for guidance regarding its form and content.)

Table 2
Comparison of the Weighted Oscillator Strengths gf Between the Present and Previous Calculations for Fe XIV

$i-j$	AS	FAC	SMY[a]	Tayal[b]	FTI[c]	$i-j$	AS	FAC	SMY[a]	Tayal[b]	FTI[c]
1–3	1.46^{-3} [d]	1.47^{-3}	1.58^{-3}		1.57^{-3}	3–95	2.31^{-5}	2.18^{-5}			3.89^{-5}
1–4	6.21^{-5}	5.93^{-5}	6.27^{-5}		5.82^{-5}	4–13	8.28^{-3}	7.19^{-3}	1.14^{-2}		1.04^{-2}
1–6	1.63^{-1}	1.58^{-1}	1.60^{-1}	1.63^{-1}	1.65^{-1}	4–14	2.20^{-4}	2.23^{-4}	2.32^{-4}		
1–8	4.01^{-1}	3.98^{-1}	4.01^{-1}	3.82^{-1}	3.84^{-1}	4–15	5.69^{-1}	5.73^{-1}	5.60^{-1}	5.76^{-1}	5.70^{-1}
1–9	2.85^{-1}	2.84^{-1}	2.63^{-1}	2.94^{-1}	2.96^{-1}	4–16	3.98^{-3}	3.36^{-3}	4.93^{-3}	4.24^{-3}	9.31^{-4}
1–10	2.96^{-1}	2.98^{-1}	2.90^{-1}	2.94^{-1}	2.96^{-1}	4–17	4.49^{-4}	4.29^{-4}	4.44^{-4}		
1–11	9.80^{-1}	9.83^{-1}	9.53^{-1}	9.72^{-1}		4–18	7.97^{-3}	8.08^{-3}	8.42^{-3}	7.24^{-3}	7.68^{-3}
1–47	6.69^{-6}			3.48^{-5}		4–19	1.51^{-2}	1.60^{-2}			
1–48	9.59^{-6}	1.56^{-5}		7.24^{-6}		4–22	1.11^{+0}	1.09^{+0}	1.11^{+0}	1.10^{+0}	1.09^{+0}
1–56	1.63^{-4}	2.26^{-4}		1.55^{-4}		4–23	1.70^{-1}	1.59^{-1}	1.88^{-1}	1.63^{-1}	1.62^{-1}
1–60	2.30^{-4}	3.56^{-4}		2.56^{-4}		4–24	9.56^{-3}	8.20^{-3}	1.35^{-2}	8.52^{-3}	8.94^{-3}
1–61	4.83^{-4}	7.69^{-4}				4–25	3.88^{-1}	3.90^{-1}	3.77^{-1}	3.90^{-1}	3.88^{-1}
2–3	6.62^{-4}	6.59^{-4}	6.97^{-4}		7.25^{-4}	4–27	5.65^{-1}	5.72^{-1}	5.34^{-1}	5.72^{-1}	5.68^{-1}
2–4	7.62^{-4}	7.57^{-4}	8.15^{-4}		7.85^{-4}	4–28	4.33^{-1}	4.38^{-1}	3.98^{-1}	4.44^{-1}	4.42^{-1}
2–5	4.47^{-3}	4.38^{-3}	4.77^{-3}		4.55^{-3}	4–29	1.65^{-3}	2.66^{-3}	1.40^{-3}		
2–6	6.38^{-3}	6.13^{-3}	5.58^{-3}	6.72^{-3}	6.62^{-3}	4–30	1.87^{-2}	2.08^{-2}	1.93^{-2}		1.84^{-2}
2–7	2.21^{-1}	2.16^{-1}	2.15^{-1}	2.24^{-1}	2.25^{-1}	4–31	2.44^{-3}	2.60^{-3}	2.52^{-3}		
2–8	3.51^{-2}	3.69^{-2}	2.88^{-2}	4.04^{-2}	4.05^{-2}	4–93	1.02^{-5}	1.31^{-5}			1.05^{-5}
2–9	4.65^{-1}	4.70^{-1}	4.61^{-1}	4.60^{-1}	4.63^{-1}	4–95	6.58^{-5}	4.88^{-5}			5.94^{-5}
2–10	1.41^{+0}	1.42^{+0}	1.38^{+0}	1.41^{+0}	1.41^{+0}	5–13	3.20^{-2}	2.87^{-2}	3.96^{-2}		3.84^{-2}
2–11	2.36^{-1}	2.38^{-1}	2.32^{-1}	2.35^{-1}		5–14	7.23^{-3}	6.72^{-3}	7.49^{-3}		8.72^{-3}
2–12	1.75^{+0}	1.76^{+0}	1.71^{+0}	1.75^{+0}		5–15	8.12^{-1}	8.24^{-1}	7.97^{-1}	8.28^{-1}	8.14^{-1}
3–13	1.07^{-2}	9.59^{-3}	1.34^{-2}		1.23^{-2}	5–16	8.71^{-6}	3.75^{-5}	2.08^{-7}		2.77^{-3}
3–15	2.88^{-1}	2.90^{-1}	2.83^{-1}	2.92^{-1}	2.88^{-1}	5–18	4.52^{-3}	4.47^{-3}	4.89^{-3}	4.13^{-3}	4.43^{-3}
3–16	6.82^{-4}	8.67^{-4}	5.28^{-4}	4.68^{-4}	2.24^{-3}	5–19	7.44^{-3}	7.58^{-3}			9.55^{-3}
3–17	2.85^{-4}	2.42^{-4}	2.91^{-4}			5–20	1.96^{-2}	1.99^{-2}	2.10^{-2}	1.76^{-2}	1.90^{-2}
3–19	7.13^{-3}	7.28^{-3}				5–22	1.25^{-1}	1.31^{-1}	1.06^{-1}	1.31^{-1}	1.30^{-1}
3–23	7.86^{-1}	7.82^{-1}	7.71^{-1}	7.84^{-1}	7.83^{-1}	5–23	2.91^{-2}	3.17^{-2}	2.21^{-2}	3.12^{-2}	2.99^{-2}
3–24	5.60^{-1}	5.57^{-1}	5.51^{-1}	5.58^{-1}	5.57^{-1}	5–26	2.33^{+0}	2.31^{+0}	2.28^{+0}	2.33^{+0}	2.31^{+0}
3–25	7.26^{-4}	1.18^{-3}	1.51^{-5}	1.06^{-3}		5–27	3.41^{-1}	3.36^{+0}	3.41^{-1}	3.40^{-1}	3.39^{-1}
3–27	1.08^{-3}	1.84^{-3}	9.49^{-6}	1.67^{-3}		5–28	1.16^{+0}	1.15^{+0}	1.15^{+0}	1.15^{+0}	1.14^{+0}
3–29	1.08^{-2}	1.11^{-2}	1.20^{-2}		1.07^{-2}	5–30	2.39^{-3}	4.61^{-4}	4.09^{-3}		
3–33	4.96^{-3}	5.66^{-3}	5.07^{-3}			5–31	1.27^{-3}	1.40^{-3}	1.29^{-3}		
3–34	1.11^{-3}	1.30^{-3}	1.10^{-3}			5–32	1.90^{-2}	2.02^{-2}	1.96^{-2}		1.87^{-2}
3–37	1.20^{-6}		8.07^{-6}			5–35	1.19^{-2}	1.23^{-2}	1.17^{-2}		1.14^{-2}
3–38	1.16^{-5}		7.23^{-6}			5–91	4.80^{-5}	6.10^{-5}			4.55^{-5}
3–39	3.48^{-5}		1.66^{-5}			5–95	5.54^{-6}	...			7.34^{-6}
3–93	2.42^{-5}	2.28^{-5}			4.26^{-5}						

Notes. The indices (i, j) correspond to the levels as shown in Table 1.
[a] SMY refers to the results of Storey et al. (2000).
[b] Tayal refers to the calculation of Tayal (2008) using the MCHF method.
[c] FTI denotes the result of Froese Fischer et al. (2006) with the MCHF method.
[d] x^y denotes $x \times 10^y$.

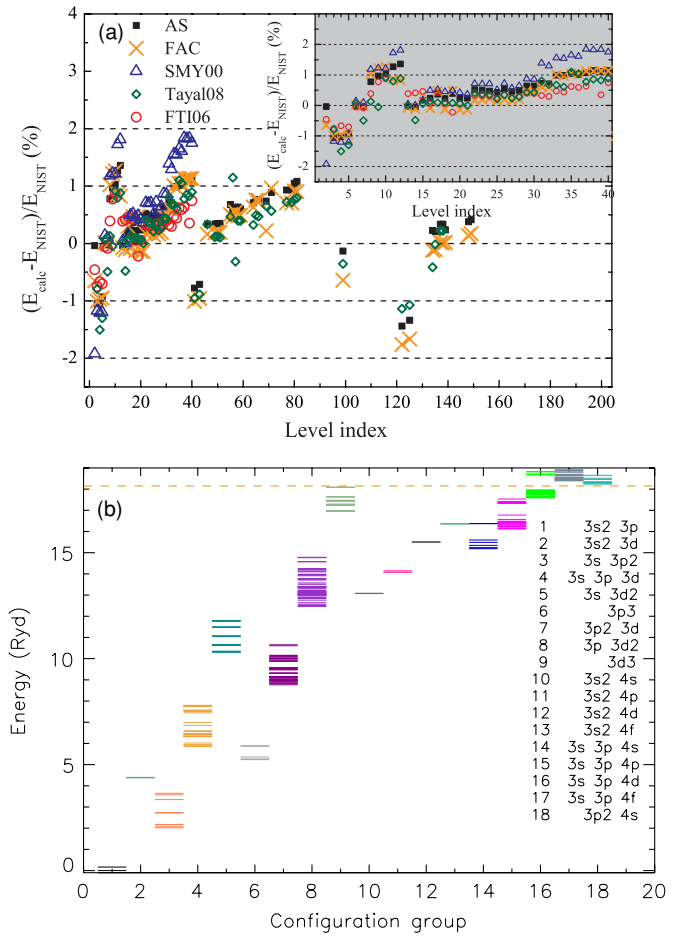

Figure 1. (a) Comparison of the level energies of Fe^{13+} from various theoretical calculations and the experimentally derived data available from the NIST database (see footnote 8). AS and FAC denote the present AUTOSTRUCTURE and FAC calculations. SMY00 refers to the calculation of Storey et al. (2000) using the SUPERSTRUCTURE code; Tayal08 and FTI06 refer to the work of Tayal (2008) and Froese Fischer et al. (2006), respectively, using the MCHF method. Level index refers to the ID number listed in Table 1. Horizontal dashed lines correspond to the degree of agreement within 0%, 1%, and 2%. The inset panel shows the data for levels below the 40th. (b) The whole set of energy levels included in the present close-coupling expansion (below the horizontal dashed line) as well as some levels of the correlation configurations $3s3p4f$ and $3p^24s$.
(A color version of this figure is available in the online journal.)

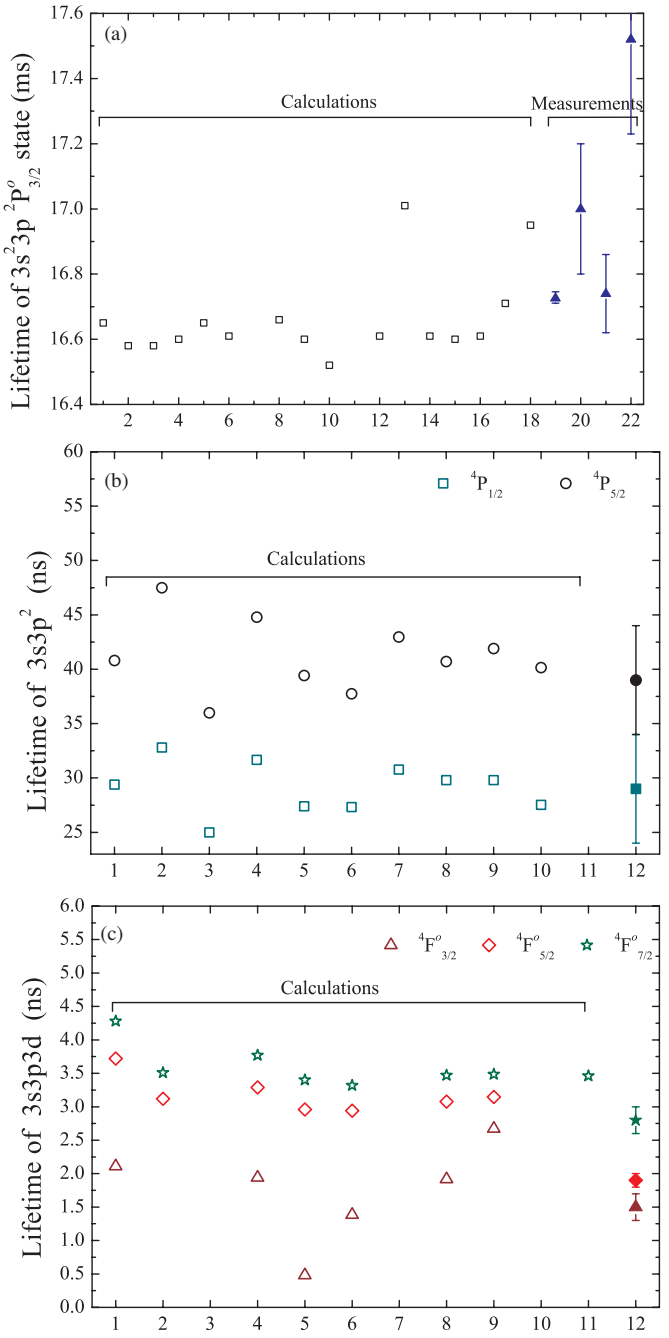

Figure 2. Comparison of lifetime between measurements (data with error bars) and various theoretical calculations. The numbers on the *x*-axis label the results obtained by different theoretical and experimental groups. (a) 1–14 taken from Table 2 in the work of Brenner et al. (2007); 15: Storey et al. (2000); 16: NIST (see footnote 8); 17 and 18: the present AS and FAC, respectively; 19: Brenner et al. (2007, HD-EBIT); 20: Smith et al. (2005, Kingdon trap); 21: Beiersdorfer et al. (2003, LLNL-EBIT); 22: Moehs & Church (1999, Kingdon trap). (b and c) 1: Huang (1986); 2: Froese Fischer & Liu (1986); 3: Träbert et al. (1988, and references therein); 4 and 5: Gupta & Msezane (2001, ab initio and adjusted energy, respectively); 6: Storey et al. (2000); 7: Tayal (2008); 8 and 9: the present AS and FAC, respectively; 10: Froese Fischer et al. (2006); 11: Dong et al. (2006); 12: Träbert et al. (1988, 1993, Experimental data).
(A color version of this figure is available in the online journal.)

& Church 1999), measured with an electrostatic Kingdon trap of the University of Nevada, is significantly longer than theoretical values, including the present AS value (16.71 ms). An updated value (17.0 ± 0.2 ms) by Smith et al. (2005) obtained at a similar facility at the Jet Propulsion Laboratory shows good agreement with the present FAC calculation (16.95 ms), but is still slightly higher than the present AS calculation and other theoretical results as shown in Figure 2. The measurement (16.74 ± 0.12 ms) at the Livermore EBIT by Beiersdorfer et al. (2003) shows good agreement with the present AS data but is slightly higher than other theoretical calculations. A recent high precision measurement ($16.726^{+0.020}_{-0.010}$ ms) has been made by Brenner et al. (2007) at Heidelberg EBIT showing excellent agreement with the present AS calculation.

For some higher excited levels, such as $3s3p^{24}P_{1/2,5/2}$ and $3s3p3d^4F^o_{3/2,5/2,7/2}$, experimental data for the lifetimes are available in the works of Träbert et al. (1988, 1993). A comparison of the lifetimes for the $3s3p^{24}P_{1/2,5/2}$ levels indicates that the present AS results are similar to the previous calculations and are also in agreement with laboratory measurements. For the $3s3p3d^4F^o_{5/2,7/2}$ levels, the present AS lifetimes agree closely with the other theoretical results and are slightly higher than the experimental data for the $^4F^o_{7/2}$ level. For the $^4F^o_{5/2}$

level, all theories are higher than the measurement by at least 60%. On the other hand, the various theoretical values for the $3s3p3d^4\,F^{o}_{3/2}$ lifetime show more scatter.

2.3. Scattering

The scattering calculations were performed using a suite of parallel ICFT *R*-matrix codes (Griffin et al. 1998). We employed 40 continuum basis orbitals per angular momentum so as to represent the $(N + 1)$th scattering electron. All partial waves from $J = 1$ to $J = 41$ were included explicitly and the contributions from higher J values were taken into account using a "top-up" procedure (Burgess 1974; Badnell & Griffin 2001). The contributions from the partial waves up to $J = 12$ were included in the exchange *R*-matrix calculation, while that from $J = 13$ to 41 was included via a non-exchange *R*-matrix calculation. In the exchange calculation, a fine energy mesh of $1.0 \times 10^{-5}\,q^2$ Ryd was used up to 29.9 Ryd, where $q = 13$ is the effective charge of the ion. This is sufficient to resolve the majority of the resonances in the closed channel region. Above 29.9 Ryd and up to three times the ionization potential of this ion, a coarser energy mesh ($2.0 \times 10^{-3}\,q^2$ Ryd) was employed. In the non-exchange calculation, a step of $2.0 \times 10^{-3}\,q^2$ Ryd was applied over the entire energy range.

For energies greater than three times the ionization potential, we used the scheme described by Burgess & Tully (1992) in which reduced collision strengths are interpolated between the *R*-matrix results and limiting high-energy behaviors. The necessary Born limits for non-dipole transitions and line strengths for dipole transitions were obtained from the AS target calculation. Finally, the thermally averaged collision strengths (Υ) were generated at 13 electron temperatures ranging from $2\times10^2(q+1)^2$ K to $2 \times 10^6(q + 1)^2$ K. The data were stored in the ADAS adf04 format (Summers 2004) being available electronically from the OPEN-ADAS database[9] and APAP network (see footnote 6).

Hossain et al. (2007) performed an absolute measurement of the electron-impact excitation cross section for the fine-structure levels of the ground term: $3s^23p^2\,P^{o}_{1/2}$ to $^2P^{o}_{3/2}$. The energy resolution in their measurement is best represented by a ∼0.125 eV full width at half-maximum (FWHM) Gaussian profile. In Figure 3, we compare our convoluted results with the measured ones and with the theoretical results of Storey et al. (2000) and Tayal (2008). The peak of the near-threshold resonance feature in Storey et al.'s data is higher by up to a factor of two than the present ICFT and Breit–Pauli (Tayal 2008) *R*-matrix results, and the experimental value. The present resonance strength is in quite good agreement with Tayal's data and also shows similar structure. On the other hand, both are higher than the measured value, by ∼80% and ∼70%, respectively. Our resultant Υ is in good agreement with Tayal's over the entire temperature range shown. The significant overestimation of the cross section in the calculation of Storey et al. (2000) is probably due to the methodology used, viz. the JAJOM code and term-coupling coefficients (TCC), as noticed in Fe^{15+} by Liang et al. (2008). This deficiency is eliminated at root by the ICFT *R*-matrix method by its use of the complete MQDT collision matrices at all energies. The Storey et al. (2000) Υ is higher than the present ICFT data by 33% at $T_e = 1.0 \times 10^6$ K and 28% at $T_e = 2 \times 10^6$ K.

In Figure 4, we make an extensive comparison of the present Υ from the ground level $3s^23p^2\,P_{1/2}$ with the data of Storey et al. (2000) obtained with the *R*-matrix with JAJOM methodology and

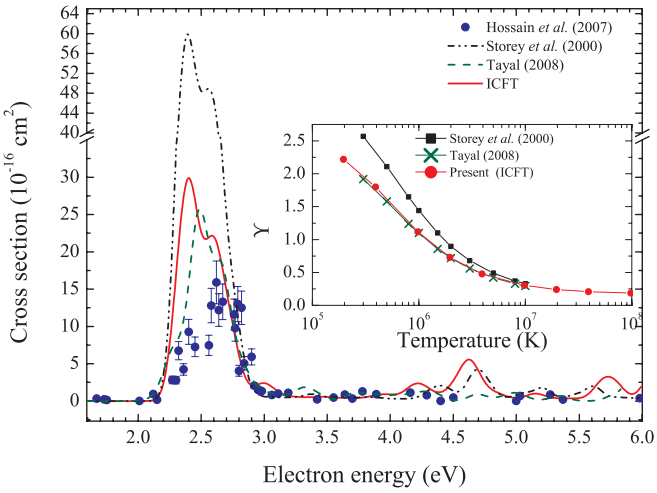

Figure 3. Comparison of the excitation cross sections of the convolved (Gaussian profile with the FWHM of 0.125 eV) 135-level Breit–Pauli *R*-matrix (Tayal 2008), 40-level JAJOM *R*-matrix (Storey et al. 2000), and the present 197-level ICFT *R*-matrix results with absolute experimental cross sections (Hossain et al. 2007) for the coronal "green" line transition ($3s^23p^2P^{o}_{3/2} \rightarrow 3s^23p^2P^{o}_{1/2}$). The inset panel shows a comparison of the Maxwellian-averaged collision strengths (Υ).

(A color version of this figure is available in the online journal.)

with Tayal (2008) who used the Breit–Pauli *R*-matrix method. At the temperature of $T_e = 2.0 \times 10^6$ K of peak abundance of Fe^{13+} in ionization equilibrium (Bryans et al. 2009), ∼51% and 59% of the available excitation data from the ground state show agreement within 30% when compared with data of Storey et al. (2000) and Tayal (2008), respectively. We also notice a trend that the Υ ratio between Storey et al. (2000) and the present ICFT decreases with decreasing of collision strength, that is presumably due to the lack of resonances as discussed below. At a low temperature of $T_e = 3.0\times10^5$ K, the percentage is 51% and 43%, respectively. At a high temperature of $T_e = 1.0 \times 10^7$ K, the percentage increases up to 62% and 71%, respectively. For some transitions (e.g., points with "+" symbols in Figure 4), the present data agree well with calculations of Storey et al. (2000) at the high temperature. However, the results of Tayal (2008) are significantly lower (a factor of ∼2) than the present calculations. For some transitions, both previous calculations are lower than the present data at the high temperature. We select one transition (labeled by the "×" symbol) with a large difference in Figure 4 to look for any underlying problem. The transition is for $3s3p3d^2\,P^{o}_{3/2} \rightarrow 3s^23p^2\,P_{1/2}$ (39-1), which is non-dipole, and its results are shown in Figure 5. Because the original collision strengths Ω of Tayal (2008) are not available, only a comparison with the data of Storey et al. (2000) is shown here. There are no resonances in the calculations of Storey et al. (2000) due to the small scale of their calculation. The strong resonances are attached to $3p^23d$, $3d^3$, and $3l3l'4l''$ levels, which they did not include. However, the background in Storey et al.'s data is significantly lower than the present calculations. This difference extends to the high energy (Born) limit, see the symbols in Figure 5. The Υ ratio between the present calculation and that of Tayal (2008) for this transition is also quite low (∼0.22; see Figure 4).

3. COLLISIONAL-RADIATIVE MODEL

In order to perform line identifications and spectroscopic diagnostics in astrophysical and laboratory plasmas, it is necessary

[9] http://open.adas.ac.uk

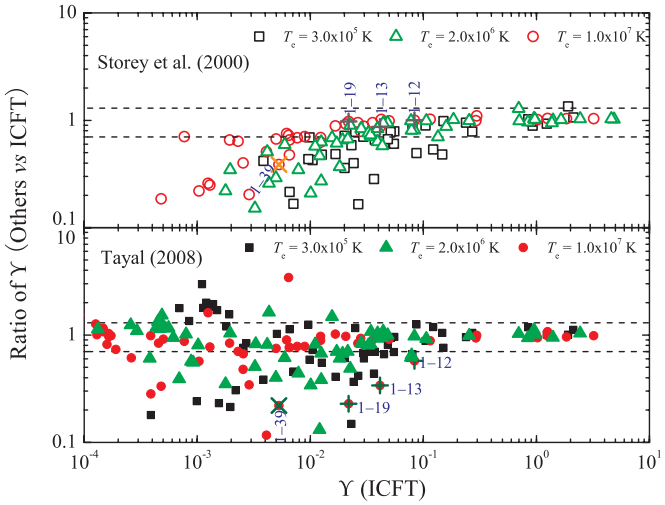

Figure 4. Extensive comparison (all available excitation data from the ground state) of effective collision strengths Υ between the present ICFT and Breit–Pauli *R*-matrix data (Tayal 2008, solid symbols) as well as data of Storey et al. (2000, open symbols) with the JAJOM approach, at temperatures of $T_e = 3.0 \times 10^5$, 2.0×10^6 (peak fraction in the ionization equilibrium of Bryans et al. 2009), and 1.0×10^7 K. For transitions of interest in the EUV region, see Figure 6(a). The points with the "×" symbol indicate the Υ ratio for the $3s^2 3p^2 P^o_{1/2} \rightarrow 3s3p3d^2 P^o_{3/2}$ transition. The points with the "+" symbol refer to transitions as labeled in the figure. The horizontal dashed lines correspond to agreement within 30%.

(A color version of this figure is available in the online journal.)

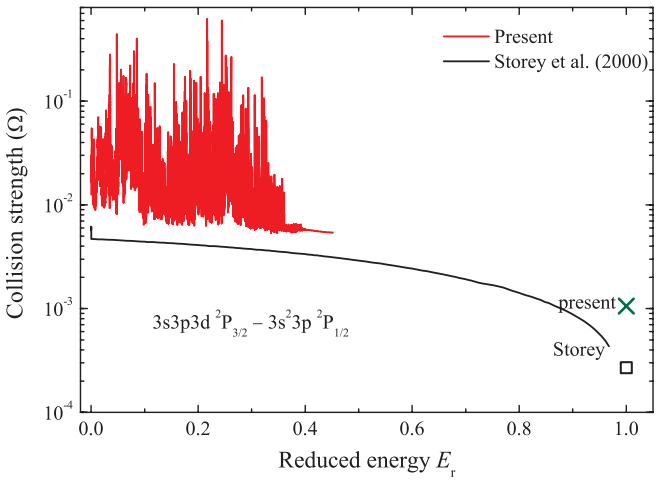

Figure 5. Comparison of the collision strength (Ω) for the $3s3p3d^2 P^o_{3/2} \rightarrow 3s^2 3p^2 P^o_{1/2}$ (39-1) transition (non-dipole, corresponding to the point with "×" symbols in Figure 4). The "×" and "□" symbols at the right-hand side denote the infinite-energy Born limit. (The reduced energy is defined by $E_r = \frac{E_j/E_{1,39}}{E_j/E_{1,39}+C}$, where E_j is the scattered electron energy in Ryd and C is an adjustable parameter—here $C = 2.0$).

(A color version of this figure is available in the online journal.)

first to know the excited level populations N_j of the emitting ion, because of its direct relation to the line emissivity $\epsilon_{j,i}$: $\epsilon_{j,i} = N_j A_{j,i} h\nu_{j,i}$, where $A_{j,i}$ is the radiative decay rate of a given $j \rightarrow i$ transition. In the present work, the calculation of the excited level populations is carried out with the ADAS package (Summers 2004; Summers et al. 2006), which is an integrated set of computer codes, including atomic models, spectroscopic simulation codes and data collections, which were developed for modeling the radiation from atoms and ions in astrophysical and fusion plasmas and for assisting in the analysis and interpretation of observed spectra.

In the present analysis, we use ADAS to analyze the soft X-ray and EUV spectra of stellar coronae and the EUV spectra measured at the Heidelberg EBIT. As the electron density is not so high and also the electron energy is high, an isolated-ion approximation can be used for determination of the excited level population by solving a system of the following coupled equations given by

$$\frac{dN_j}{dt} = \sum_{i<j} N_i n_e q_{i\rightarrow j} + \sum_{k>j} N_k (n_e q_{k\rightarrow j} + A_{k\rightarrow j}) - N_j \left(\sum_{i<j} (n_e q_{j\rightarrow i} + A_{j\rightarrow i}) + n_e \sum_{k>j} q_{j\rightarrow k} \right), \quad (1)$$

and

$$\sum_j N_j = N, \quad (2)$$

where N_j is the population number density of state j, N is the total number density of the ion, n_e is the free-electron density, and $q_{i\rightarrow j}$ is the excitation ($i < j$) or de-excitation ($i > j$) rate from the state i to j, which is simply related to the effective collision strength Υ (for Maxwellians) in cgs units by

$$q_{i\rightarrow j} = \frac{8.63 \times 10^{-6}}{g_i T_e^{1/2}} \Upsilon_{i\rightarrow j} \exp(-E_{ij}/kT_e), \quad (3)$$

where g_i is the statistical weight of level i, T_e is the electron temperature in Kelvin, and E_{ij} is the transition $j \rightarrow i$ energy.

Using the atomic data, including experimental level energies where available to correct the theoretical line wavelengths, radiative decay rates, and excitation/de-excitation rates as well as the quasi-static approximation for the excited levels ($dN_j/dt = 0$), we can obtain the level populations. In the modeling of astrophysical spectra, the proton-impact excitation rate (Heil et al. 1983) of the metastable ($3s^2 3p^2 P^o_{3/2}$) level from the ground ($^2P^o_{1/2}$) level is included with the typical proton density of $0.85 n_e$ in the stellar corona. We note that most Υs stored in the ADAS database are Maxwellian averaged. For any non-thermal electron energy distribution, such as that occurs in EBIT plasmas, we tailor the input of excitation data (with the same adf04 format) to each specific case for use with ADAS. When we analyzed the EUV spectra measured at the Heidelberg EBIT, we generated another adf04 file for use with monoenergetic electron beams, in this case a Gaussian profile with the FWHM of 30 eV.

4. LINE INTENSITY RATIOS

4.1. The EUV Spectrum

The transition scheme for emission lines arising from $3s \rightarrow 3p$ and $3p \rightarrow 3d$ excitations and the relative excitation rates and radiative decay rates are shown in Figure 6. Some of the lines have been recorded in solar active regions, as observed by SERTS on 1989 May 5 (Thomas & Neupert 1994), and by a grazing-incidence rocket spectrometer flown on 1969 April 4 (Malinovsky & Heroux 1973), as well as by the ongoing *Hinode*/EIS observations (Brown et al. 2008). It is well established that the intensities of all the SERTS-89 second-order lines were not accurate, and large discrepancies between

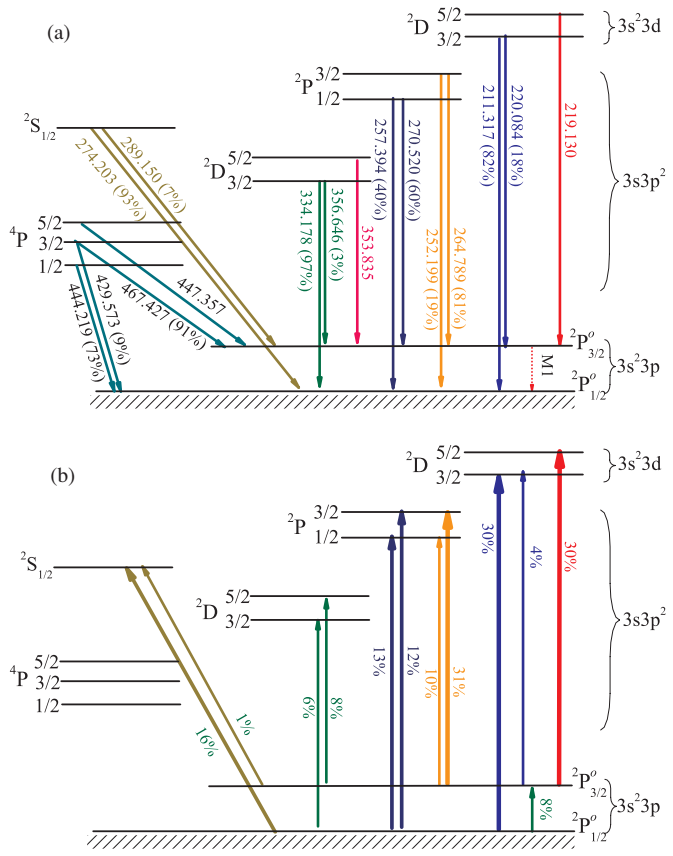

Figure 6. Scheme of the level populations for the 12 lowest-lying levels of $3s^23p$, $3s3p^2$, and $3s^23d$ configurations of Fe^{13+}. (a) Wavelengths (in Å) and branching ratios given as percentages—those larger than 1% are indicated. (b) Relative magnitudes of collisional excitation strengths at $\log T_e$ (K) = 6.3 are given in percentages, as well as being represented by the thickness of the corresponding solid lines.

(A color version of this figure is available in the online journal.)

the reported and predicted values are found (Del Zanna 1999). It has also been suggested by Young et al. (1998) that all lines in the 430–450 Å region have incorrect observed intensities, being too low by a factor of two or so, although this needs to be confirmed using more recent atomic data. The observational data by Malinovsky & Heroux (1973) were photometrically calibrated, making this the best EUV spectrum in terms of line intensities, with an accuracy of the order of 10%. The *Hinode*/EIS spectrometer was calibrated end-to-end on the ground, but only few measurements were possible. The absolute calibration was estimated to be accurate to within 20% (Lang et al. 2006). It is generally thought that the relative calibration should be accurate to better than 10%. However, it appears that various corrections at the 20% level are actually needed in some spectral ranges (Del Zanna & Ishikawa 2009; Del Zanna 2010). This is also clear by looking at the branching ratios, which we discuss below. For the *Hinode*/EIS observations, we use the compilation of line intensities in the works of Brown et al. (2008) and the present results for three different regions, i.e., quiet-Sun (QS) off-limb (Del Zanna 2010), the core of an active region (AR), and the footpoint region of a small flare clearly visible in Fe XVII (Del Zanna & Ishikawa 2009). In the observation of the footpoint region of the small flare, where chromospheric evaporation occurred, the electron density is relatively high (high n_e).

The intensity ratios of optically thin lines originating from the same upper level are proportional to the so-called branching ratios. As is clear from the assessment of the atomic structure mentioned above, the present oscillator strengths (gf) show excellent agreement with those of Storey et al. (2000) and, as seen in Table 3, most of the calculated branching ratios agree reasonably well with the solar observations. The five theoretical values for the ratio λ257.394/λ270.520 are in good agreement but generally somewhat larger than the observed values which show more scatter. The effect of proton-impact excitation was found to be negligible (0.5%) for the intensity ratios in Table 3. We now discuss the possible contributions of line blending to the intensity ratios in Table 3.

λ270.520 can be blended with Mg VI 270.394 Å, but this should not be a source of significant uncertainty in the observations of Brown et al. (2008), particularly in the active region (AR1) and limb data where Mg VI is relatively weak.

λ257.394 lies very close to the Ar XIV line at 257.37 Å, but these two lines cannot be resolved as can be seen in Figure 1 of Brown et al. (2008). The Ar XIV contribution is, however, expected to be small, particularly in active regions. Overall, the uncertainty due to blending in the λ257.394/λ270.520 ratio derived from the *Hinode*/EIS observations is expected to be small. All of the values of this ratio derived from the observations of Brown et al. (2008) are, nonetheless, smaller than the theoretical values. The same is true of the present *Hinode*/EIS observations, with the exception of the QS off-limb data where the ratio agrees well with theory.

λ264.789: Del Zanna (2010) benchmarked the atomic data of Fe^{10+} and predicted a new strong Fe XI line around 264.784 Å based on recent Iron Project calculations (Del Zanna et al. 2010). In the present *Hinode*/EIS observations (Table 3), we have taken this contribution into account in the line ratio λ252.199/λ264.789. In the QS off-limb spectrum, about 30% of the observed intensity at 264.789 Å is caused by the newly identified Fe XI transition line. In the AR observation, its contribution is about 3%.

λ289.150 appears to be blended in the QS off-limb observation (Del Zanna 2010), which may be a contribution from the C IV line at 289.228 Å ($1s^24d^2D_{5/2} \rightarrow 1s^22p^2P^o_{3/2}$), although this is predicted to be small.

λ274.203 is known to be blended with an Si VII line at 274.175 Å due to the $2s2p^5{}^3P^o_0 \rightarrow 2s^22p^4{}^3P_1$ transition, which is electron-density-sensitive. Hence, its contribution can be estimated if the electron density is known. We did so by using the observed intensity of another, unblended, Si VII line at 275.353 Å and the CHIANTI v6 (Dere et al. 2009) atomic data for this ion. In the active region, the observed ratios of Fe XIV in Brown et al. (2008) show good agreement with the present calculations, indicating that any contamination from Si VII is negligible for the active regions.

The λ274.203/λ211.217 ratio: for the present observations of the QS off-limb, the active region and the footpoint of the small flare (high n_e; Del Zanna 2010), the observed values agree with the present model prediction. However, in the observations of Brown et al. (2008), the λ274.203/λ211.217 ratio after deblending of the Si VII line is 1.76 and 1.10 in limb and limb+20″, which is still significantly higher than other observations. The reason for the large differences is not clear. In the SERTS-89 solar observation, a higher electron density of $\log n_e$ (cm^{-3}) = 10 is adopted to estimate the Si VII contribution to the 274.203 Å feature. However, it turns out that the Si VII contamination is very small, and that the ratio shows only a small change, from 1.01 ± 0.18 to 0.98 ± 0.18, which is still significantly higher than the predictions of Storey et al. (2000) and the present model, as well

Table 3
Observed Intensity Ratios of Lines from a Common Upper Level (Columns 2–6) and Electron-density-insensitive Line Intensity Ratios (Columns 7–10) of EUV Lines for Different Observations, Along with Laboratory (EBIT) Measurement and Theory

Index	$\frac{\lambda 220.084}{\lambda 211.317}$	$\frac{\lambda 252.199}{\lambda 264.789}$	$\frac{\lambda 257.394}{\lambda 270.520}$	$\frac{\lambda 289.150}{\lambda 274.203}$	$\frac{\lambda 356.645}{\lambda 334.178}$	$\frac{\lambda 274.203}{\lambda 211.317}$	$\frac{\lambda 334.178}{\lambda 274.203}$	$\frac{\lambda 444.219}{\lambda 334.178}$	$\frac{\lambda 270.520}{\lambda 264.789+\lambda 274.203}$
					Observations				
SERTS-89	0.25 ± 0.07	0.18 ± 0.06	0.38 ± 0.09	0.072 ± 0.024	0.028 ± 0.010	1.01 ± 0.18	0.62 ± 0.10	0.018 ± 0.005	0.24 ± 0.04
BFS08-QS		0.20	0.42	0.040		0.55			0.23
BFS08-AR1		0.18	0.53	0.048		0.46			0.24
BFS08-AR2		0.20	0.62	0.042		0.44			0.22
BFS08-Limb		0.21	0.50	0.054		1.76			0.27
BFS08-Limb + 20″		0.19	0.53	0.040		1.10			0.26
Present-QS off Limb		0.21[a]	0.71	0.100[b]		0.40[b]			0.23[b]
Present-AR		0.20[a]	0.52	0.050[b]		0.46[b]			0.26[b]
Present-high n_e		0.21[a]	0.54	0.050[b]		0.46[b]			0.23[b]
MH73	0.28	0.26		0.060		0.60			0.26
					Laboratory (EBIT) measurements				
$E_e = 325$ eV	0.23 ± 0.07	0.12 ± 0.07[c]	0.57 ± 0.14[d]			0.49 ± 0.09			0.20 ± 0.03
$E_e = 350$ eV	0.17 ± 0.03	0.20 ± 0.03[c]	0.55 ± 0.06[d]			0.51 ± 0.08			0.20 ± 0.02
$E_e = 375$ eV	0.15 ± 0.02	0.22 ± 0.03[c]	0.61 ± 0.05[d]			0.50 ± 0.08			0.19 ± 0.03
$E_e = 400$ eV	0.17 ± 0.02	0.21 ± 0.03[c]	0.58 ± 0.04[d]			0.51 ± 0.08			0.20 ± 0.02
					Theory				
BRS95	0.22	0.23	0.71	0.095	0.038	0.37	0.63		0.35
YLT98	0.21	0.24	0.74	0.089	0.036	0.35 ± 0.03	0.69 ± 0.07	0.015 ± 0.002	
SMY00	0.22	0.24	0.66	0.061	0.029	$0.53^{+0.05}_{-0.03}$	$0.64^{+0.06}_{-0.04}$	$0.028^{+0.011}_{-0.009}$	$0.26^{+0.02}_{-0.01}$
T08	0.21	0.24	0.73	0.091	0.034				
Present	0.21	0.24	0.70	0.076	0.032	0.55	0.70	0.032	0.27

Notes. SERTS-89 is from the data of Acton et al. (1985), BFS08 refers to the work of Brown et al. (2008), MH73 denotes the work of Malinovsky & Heroux (1973), BRS95 is the theoretical work of Brickhouse et al. (1995), YLT98 represents the analysis of Young et al. (1998), SMY00 refers to the work of Storey et al. (2000), and T08 is from the results of Tayal (2008).
[a] The contribution from Fe XI λ264.784 to the intensity of the 264.789 Å line has been taken into account.
[b] The contribution from Si VII λ274.175 to the intensity of the 274.203 Å line has been taken into account.
[c] The contribution from Fe XIII λ251.956 to the intensity of the 252.199 Å line has been taken into account according to the theoretical ratio (1.58) and intensity of another Fe XIII line at 256.422 Å due to the $3s3p^3\,^1P_1 \rightarrow 3s^23p^2\,^1D_2$ transition.
[d] Taking into account the contribution from Fe X at 257.259 Å.

as some *Hinode*/EIS observations. As suggested by Brickhouse et al. (1995) and Storey et al. (2000), the calibration uncertainty (50%) in SERTS-89 observations over a long wavelength range may be one of the reasons for such a discrepancy.

For the line intensity ratio of λ444.219/λ334.178 in the long wavelength range, the SERTS-89 observation is lower than the predictions of Storey et al. (2000) and the present work by 50% but, in contrast, that of λ334.178/λ274.203 is in agreement with the predictions of Storey et al. (2000) and the present calculation.

In summary, the ratios of line intensities in the short wavelength region can be explained satisfactorily by the present model. For the ratios of such lines over a longer wavelength range, the present results agree with those of Storey et al. (2000), and suggest again that the calibration uncertainty over a large wavelength range could be the main reason for the discrepancy between the SERTS-89 observation and theories. In order to clarify these issues we have carried out systematic laboratory measurements to establish a benchmark for some of the line ratios.

4.1.1. Laboratory Measurement—EBIT

Using the FLASH-EBIT (Epp et al. 2007; Liang et al. 2009a, 2009b) available in Heidelberg, Germany, we have taken a series of spectra of highly charged iron ions in the wavelength region between 150 and 240 Å at electron beam energies ranging from 170 to 500 eV with a step width of 10 eV and an electron current of 6.0–10.2 mA. A new EUV spectrometer with higher resolution (0.2–0.3 Å) than that previously described by Liang et al. (2009a, 2009b) has been installed on the FLASH-EBIT for the present measurement. Taking into account the ionization potential (361 eV) of Fe^{12+} and the negative space-charge potential (∼40 eV) resulting from the compressed electron beam at the trap center, Fe^{13+} ions with sufficient intensities are estimated to be produced at the nominal electron energy above 420 eV. We analyzed the spectra measured at electron energies of 430–500 eV (see Figure 7), and determined the measured line intensity ratios after proper corrections for spectrometer response function and also for the polarization effect at an energy of 420 eV with the electron density of 5.0×10^{10} cm^{-3} (which is typical in the Heidelberg EBIT plasmas; see Liang et al. 2009a) by using FAC.

As shown in Figure 7, two relatively weak lines at 218.177 Å ($3s3p3d^2\,F^o_{7/2} \rightarrow 3s3p^2\,^2D_{5/2}$) and 224.354 Å ($3s3p3d^2\,F^o_{5/2} \rightarrow 3s3p^2\,^2D_{3/2}$) of Fe XIV were predicted in the present model at the monoenergetic energy of 420 eV in addition to the well-known dominant lines (see the red solid line in Figure 7). Indeed, the present EBIT measurements indicate that these two lines were found to emerge in the observed spectra at an electron beam energy around 430 eV (see Figure 7) which is nearly at the same electron beam energy as the strongest line at 211.3 Å appeared. Therefore, we have some confidence that these two lines originate from Fe XIV. In a careful recheck of the solar spectrum (Malinovsky & Heroux 1973, Figure 1(c) and Table 1 in their work), indeed one of these transition lines was recorded at an observed wavelength of 218.21 Å and assigned to be an S XII line from the $2s^22p^2\,^2P_{3/2} \rightarrow 2s^22p^2\,P^o_{3/2}$ transition. Keenan et al. (2002) explored the n_e diagnostic possibilities of S XII lines, and found that this line intensity relative to that at 299.50 Å ($2s2p^2\,^2D_{5/2} \rightarrow 2s^22p^2\,P^o_{3/2}$) is sensitive to the electron density. However, the derived density is significantly lower (a factor of ∼3–4) than those obtained from other line ratios of this ion (Keenan et al. 2002, see Table 4 in their work). Thus, we believe that this discrepancy is caused by some contamination from the Fe XIV line at 218.177 Å, which cannot be resolved with the spectrometer aboard the SERTS with a resolution of 50–80 mÅ. Another predicted line at 224.354 Å may

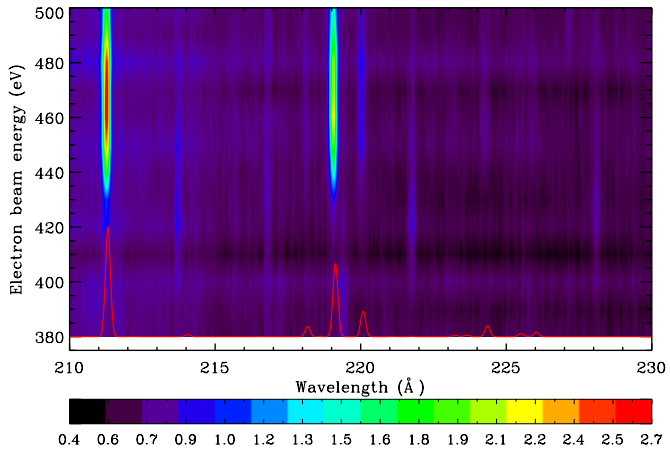

Figure 7. Two-dimensional presentation (in counts) of spectra from Fe ions observed in the wavelength range of 210.0–230.0 Å as a function of the electron impact energy (left ordinate). The electron energy shown is not corrected for the electron space charge potential. This composite image is generated by juxtaposition of a series of individual spectra from 380 to 500 eV with 10 eV intervals. The smooth curve at bottom part is the simulated spectrum of Fe XIV under monoenergetic electron impact energy of 420 eV and electron density of 5.0×10^{10} cm^{-3}.

(A color version of this figure is available in the online journal.)

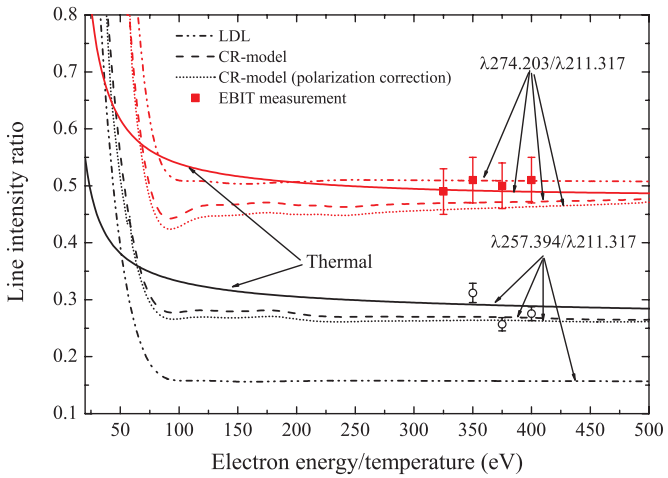

Figure 8. Line intensity ratios as a function of the electron energy (monoenergetic, Gaussian distribution with the FWHM of 30 eV) or of the temperature (thermal) at an electron density of 5.0×10^{10} cm^{-3}. The polarization correction is made with the polarization rate from a FAC calculation. LDL refers to the low-density limit as given by Equation (4). Symbols with error bars correspond to the laboratory measurements at Heidelberg EBIT.

(A color version of this figure is available in the online journal.)

also contribute to the peak around 224.4 Å in the solar observation (Malinovsky & Heroux 1973, their Figure 1(d)), which has been unknown in astrophysical sources so far, to the best of our knowledge.

A series of separate measurements of iron ions at the EBIT have been made at electron beam energies of 325, 350, 375, and 400 eV by using an EUV spectrometer (Lapierre et al. 2007; Liang et al. 2009a, 2009b) with slightly lower resolution (0.6 Å) and with a wider wavelength coverage (100–350 Å). The resultant line ratios without polarization correction are listed in Table 3 for comparison with astrophysical observations and theories. In the laboratory measurements, the emission line at 252.199 Å can be contaminated by the Fe XIII line at 251.956 Å from the $3s3p^{33}S^{o}_{1} \rightarrow 3s^{2}3p^{23}P_{2}$ transition. We adopt another Fe XIII line at 256.422 Å from the $3s3p^{31}P^{o}_{1} \rightarrow 3s^{2}3p^{21}D_{2}$ transition and the theoretical line ratio $\frac{I(\lambda 251.956)}{I(\lambda 256.422)} = 1.58$ predicted in our previous work (Liang et al. 2009a) to extract the Fe XIII contamination at 252.199 Å. The measured ratio ($\frac{\lambda 252.199}{\lambda 264.789}$) of Fe XIV is found to agree well with astrophysical observations and theories including the present work (see Table 3). For the other three line intensity ratios, e.g., $\frac{\lambda 220.084}{\lambda 211.317}$, $\frac{\lambda 274.203}{\lambda 211.317}$, and $\frac{\lambda 270.520}{\lambda 264.789+\lambda 274.203}$, the measured ratios without polarization correction are in agreement with astrophysical observations and theories (see Table 3).

In the measurements of Liang et al. (2009a, see their Figure 1(c)), we see the Fe X line at 257.259 Å ($3s^{2}3p^{4}3d^{4}D_{7/2} \rightarrow 3s^{2}3p^{52}P^{o}_{3/2}$), which cannot be resolved from the Fe XIV line at 257.394 Å with the spectrometer used. Before the deblending, the observed ratio of $\frac{\lambda 257.394}{\lambda 270.520}$ in the present EBIT measurement is a factor of 2–4 higher than others (including astrophysical observations and predictions) and also shows a clear electron energy dependence. Using the measured value of 0.26 ± 0.02 (relative to that of the strongest Fe X line at 174.526 Å) at $E = 240$ eV from the work of Liang et al. (2009a), the line intensity ratio $\frac{\lambda 257.394}{\lambda 270.520}$ reduces to 0.58 ± 0.03 in the electron beam energy range of $E_e = 325$–400 eV which is in reasonable agreement with the solar *Hinode*/EIS observations in Brown et al. (2008) and the present analysis. This further suggests that the discrepancies between the SERTS-89 observation and theories are not due to atomic physics but problems in the solar observations.

The EBIT operates under monoenergetic conditions in the present measurements with variable energy in order to resolve and identify a series of emission lines from ion species with different charge states (Liang et al. 2009a). However, the comparison of line ratios with the astrophysical observations is significantly affected by the distribution function of the electron energies, in addition to the effect of polarization (see the work of Loch et al. 2006 for Fe XVII). In Figure 8, we show the two line ratios ($\frac{\lambda 257.394}{\lambda 211.317}$ and $\frac{\lambda 274.203}{\lambda 211.317}$) under the thermal and monoenergetic Gaussian distribution with the FWHM = 30 eV at an electron density of 5.0×10^{10} cm^{-3}. This indicates that the distribution function of the exciting electron energies plays an important role in determining the line intensity ratios at low (below 150 eV) plasma electron energies. The differences between the thermal and monoenergetic electron cases decrease with increasing electron energies, and fall below 10% above 300 eV for these two line ratios. In the monoenergetic electron case, the polarization correction from a FAC calculation has been taken into account in the present model, and found to be very small for low electron energy and low electron current conditions used in the present work.

A simple model of the line intensity ratios has also been included in Figure 8. In this model, collisional de-excitation has been neglected (the low-density limit) as has radiative cascading from higher states. Excited levels are populated by direct excitation from the ground level and depopulated by radiative decay. The line emissivity ratio is then

$$\frac{\epsilon_{i\rightarrow g}}{\epsilon_{j\rightarrow g}} = \frac{q_{g\rightarrow i}}{q_{g\rightarrow j}} \frac{B_{i\rightarrow g}}{B_{j\rightarrow g}} \frac{h\nu_{ig}}{h\nu_{jg}}, \quad (4)$$

where $q_{g\rightarrow i}$ is the electron-impact excitation rate from the ground state (g) to the excited state (i), and $B_{i\rightarrow g}$ represents the branching ratio for the spontaneous radiative decay rates from the excited state (i) to the ground state (g). Figure 8 reveals that the cascade effects included in the present CR

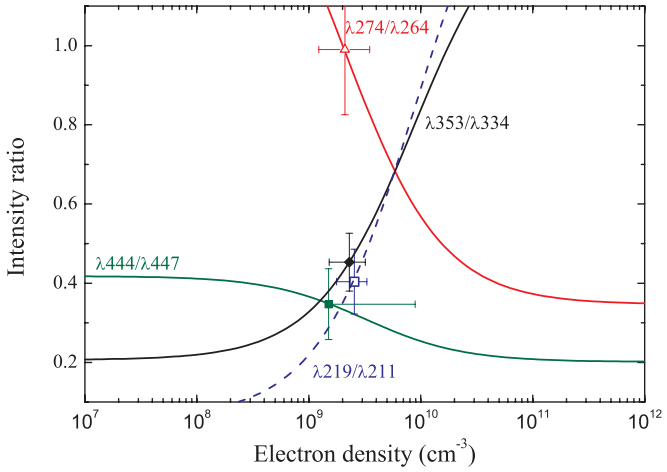

Figure 9. Line intensity ratios of different transitions as a function of the electron density at the temperature of $T_e = 2.0 \times 10^6$ K with peak fraction in equilibrium, along with observed ratios (symbols with error bars) observed in SERTS-89 corresponding to the estimated electron densities.

(A color version of this figure is available in the online journal.)

model are significant for coronal-like plasmas. Additionally, weak resonances in the predicted intensity ratio (monoenergetic) can be found below $E_e < 250$ eV, which results from resonances in the electron-impact excitation cross section.

4.1.2. Electron Density

Storey et al. (2000) and Young et al. (1998) listed several n_e-sensitive line ratios of iron ions. In the present work, we use ratios of line intensities over a narrow wavelength range to diagnose the electron density in order to avoid any effect of the spectrometer response. Using the present atomic data, the resultant (mean) electron density of the solar active region in the SERTS-89 observations, from the ratios of λ274/λ264, λ219/λ211, and λ353/λ334, is $2.3^{+0.8}_{-0.6} \times 10^9$ cm^{-3} (see Figure 9). This agrees well with the value ($2.6^{+1.9}_{-1.3} \times 10^9$ cm^{-3}) estimated by Storey et al. (2000). The effect of proton-impact excitation is found to be ∼5% or less at $n_e = 1.0 \times 10^{10}$ cm^{-3} in these density-sensitive ratios.

4.2. Soft X-ray Transition Lines

Five $n = 4 \rightarrow n = 3$ transitions have been recorded in a solar flare observation and identified by Acton et al. (1985). In the present work, we further analyzed the soft X-ray emission lines in the Procyon observations using the present atomic model. In the newest version of CHIANTI v6 (Dere et al. 2009) extensively used by the astronomical community, no data are available for the $n = 4$ levels of this ion. Thus, no soft X-ray emission lines of Fe XIV can be predicted.

4.2.1. Solar Flare

The $3s^2 4d^2 D_{3/2} \rightarrow 3s^2 3p^2 P^o_{1/2}$ line at 58.963 Å has been recorded and identified in the solar observation performed on 1969 April 4 at 1935 UT and identified by Malinovsky & Heroux (1973). In a later solar flare observation done on 1982 July 13 at 1630 UT using the Nike-boosted Black Brant V vehicle, this transition line was detected again (Acton et al. 1985). Four more lines were also recorded in that observation and identified (see Table 4). In this table, we give the theoretical relative intensities at 2.0×10^6 K, corresponding to the peak fractional abundance of Fe^{13+} (Bryans et al. 2009). Theoretical values are tabulated at electron densities of 3.2×10^8 cm^{-3}, a typical value for the corona of Procyon and 1.0×10^{10} cm^{-3}, typical of a solar flare. The upper and lower limits in the theoretical ratios represent the maximum deviation from this value over the electron density range of $1.0 \times 10^7 \text{cm}^{-3} \leqslant n_e \leqslant 1.0 \times 10^{12}$ cm^{-3}.

The emission line at 69.652 Å recorded in the solar flare observation was identified to be the Si VIII line at 69.632 Å, with a minor contribution from Fe XIV as discussed by Acton et al. (1985). In the model of Keenan et al. (2006), Fe XV can satisfactorily explain the observed intensity in the solar observation. In the present model, we predict the contribution from Fe XIV to be ∼5%. Experimental data for the $3s3p4s^4 P^o_{3/2,5/2}$ levels are available from the NIST database. Using the average difference between the present structure calculation and the NIST data for these two levels, the wavelength of the $3s3p4s^4 P^o_{1/2} \rightarrow 3s3p^{24} P_{3/2}$ transition line shifts from 69.853 Å to 70.031 Å. For the emission line at 70.05 Å, Keenan et al. (2006) reported a significant discrepancy of the intensity ratio $\frac{\lambda 70.05}{\lambda 59.40}$ between the solar observation and their model's prediction for Fe XV. The present prediction of Fe XIV at the electron density of 1.0×10^{10} cm^{-3} can provide an explanation of the difference. Taking the contribution (∼5%) from Fe XIV to the emission line at 70.05 Å, the observed intensity ratio $\frac{\lambda 70.05}{\lambda 59.40}$ of Fe XV decreases to 0.68 ± 0.21, being closer to their model prediction of 0.46 ± 0.09. The emission line at 70.60 Å recorded in the solar observation was assigned to be Fe XIV by Acton et al. (1985). The present model indicates that the contribution from Fe XIV is less than ∼50%. In the present work, we predict another density-sensitive feature at 71.376 Å (experimental wavelength) with an intensity ratio of $1.79^{+1.26}_{-1.73}$ at $n_e = 1.0 \times 10^{10}$ cm^{-3}, that is in good agreement with the solar observation. Thus, we tentatively assign the unknown emission line at 71.34 Å in the solar observation to Fe XIV. Additionally, we predict a strong line at 71.912 Å from the $3s3p4s^2 P^o_{1/2} \rightarrow 3s3p^{22} D_{3/2}$ transition using the empirically adjusted theoretical energy of the $3s3p4s^2 P^o_{1/2}$ state. Prior to this adjustment this line lies at 71.703 Å. Therefore, we believe that the emission at 71.91 Å in the solar flare observation (Acton et al. 1985) might be blended with an Fe XIV line, which was previously identified to be the Mg IX line at 71.901 Å arising from the $2s3s^3 S_1 \rightarrow 2s2p^3 P^o_1$ transition (Acton et al. 1985). Moreover, the present predicted ratio at $n_e = 1.0 \times 10^{10}$ cm^{-3} is higher than the solar observation by ∼50% (see Table 4). Two emission lines at 76.03 Å and 76.16 Å were assigned to be from Fe XIV, based upon the wavelength coincidence by Acton et al. (1985). The present model predicts comparable line intensities with solar flare observation (Acton et al. 1985) and confirms the line identifications for both. We note that another two prominent lines, at 58.979 and 78.765 Å, are predicted with comparable intensities, as listed in Table 4. The emission line at 91.01 Å was unknown from astrophysical sources so far. The present model gives good agreement with the solar observation at high electron densities. Therefore, we tentatively assign the 91.01 Å line to be the Fe XIV line from the $3s^2 4p^2 P^o_{3/2} \rightarrow 3s3p^{22} D_{5/2}$ transition, although this line is sensitive to the electron density. In summary, two emission lines at 71.34 Å and 91.01 Å, previously unknown in astrophysical observations, are identified in the soft X-ray region.

4.2.2. Procyon

In the line list of Raassen et al. (2002) for a Procyon observation, no emission lines of Fe XIV were reported. In the present work, we extract the line flux as done in the work of Liang & Zhao (2008) at the wavelengths as listed in Table 4.

Table 4
Prominent Soft X-ray Lines and their Intensity Ratios (Relative to that of the Line at 58.963 Å) Recorded in Solar (Acton et al. 1985) and Procyon (Raassen et al. 2002) Observations, Along with Theories at Low and High Density

Transitions	Theory			Observations			
		Ratio at n_e(cm^{-3})		Solar		Procyon	
	λ (Å)	1.0×10^{10}	3.2×10^{8}	λ (Å)	Ratio	λ (Å)	Ratio
$3s^23p^2\,P^o_{1/2}$–$3s^24d^2\,D_{3/2}$	−58.963	1.00	1.00	58.96	1.00	58.962	1.00
$3s3p^{24}\,P_{5/2}$–$3d3p4d^4\,D^o_{7/2}$	58.979	$0.51^{+0.09}_{-0.11}$	$0.40^{+0.20}_{-0.00}$				
$3s3p^{24}\,P_{5/2}$–$3s3p4s^4\,P^o_{5/2}$	−69.652	$0.13^{+0.07}_{-0.09}$	$0.05^{+0.15}_{-0.01}$	69.65[a]	3.01	69.639	3.77 ± 1.53
$3s3p^{24}\,P_{3/2}$–$3s3p4s^4\,P^o_{1/2}$	69.853[b]	$0.10^{+0.00}_{-0.00}$	$0.10^{+0.00}_{-0.00}$	70.05[a]	2.28	70.048	1.40 ± 0.65
$3s^23p^2\,P^o_{3/2}$–$3s^24s^2\,S_{1/2}$	−70.613[b]	$0.28^{+0.03}_{-0.05}$	$0.24^{+0.07}_{-0.01}$	70.60	0.59	70.603	1.20 ± 0.56
$3s3p^{22}\,D_{5/2}$–$3s3p4s^2\,P^o_{3/2}$	−71.376	$1.79^{+1.26}_{-1.73}$	$0.18^{+2.87}_{-0.12}$	71.34[c]	1.52		
$3s3p^{22}\,D_{3/2}$–$3s3p4s^2\,P^o_{1/2}$	71.703	$2.49^{+0.60}_{-0.45}$	$3.05^{+0.04}_{-1.01}$	71.91[d]	1.66	71.920	1.13 ± 0.52
$3s^23d^2\,D_{3/2}$–$3s^24f^2\,F^o_{5/2}$	−76.022	$1.74^{+0.90}_{-1.24}$	$0.59^{+2.05}_{-0.09}$	76.03	2.03	76.033	0.90 ± 0.62
$3s^23d^2\,D_{5/2}$–$3s^24f^2\,F^o_{7/2}$	−76.151	$0.50^{+0.10}_{-0.08}$	$0.60^{+0.00}_{-0.18}$	76.16	0.72		
$3s3p^{22}\,D_{3/2}$–$3s^24p^2\,P^o_{1/2}$	78.765	$1.00^{+0.13}_{-0.09}$	$1.12^{+0.00}_{-0.21}$			78.775	1.18 ± 0.52
$3s3p^{22}\,D_{5/2}$–$3s^24p^2\,P^o_{3/2}$	−91.008	$1.25^{+0.69}_{-0.94}$	$0.36^{+1.58}_{-0.05}$	91.01[c]	1.45	91.038	1.60 ± 0.88

Notes. A "–" symbol in the wavelength column indicates that experimentally derived level energies (NIST data, see footnote 8) were used.
[a] Blending from other features.
[b] This line intensity ratio is insensitive to n_e.
[c] Unknown emission lines.
[d] Different identification.

Because of low count rates in the Procyon observations, errors are found to be relatively large. However, it is still useful for the astronomical community in stellar X-ray physics to assess any contamination from Fe XIV lines.

As seen in Table 4, the predicted contribution from Fe XIV lines at 69.639 Å and 70.603 Å is apparently smaller than that in the solar flare observation (Acton et al. 1985). This suggests that contamination from ions produced at lower formation temperatures becomes stronger, e.g., the Si VIII line at 69.632 Å ($2p^23s^4\,P_{5/2} \rightarrow 2p^{34}\,P^o_{3/2}$) contaminates some features observed at 69.639 Å. For the emission line at 70.603 Å, the dominant contribution is still unknown. For the feature at 70.048 Å, the relative fraction from Fe XIV increases from ∼5% in the solar flare observation to ∼10% in the Procyon observation. This is caused by the reduced fractional abundance of Fe^{14+} because of the lower ionization degree in the corona of Procyon compared to a solar flare. As discussed for the solar flare observations, the present model can satisfactorily explain the observed line intensity at 71.91 Å. However, its line intensity is overestimated at low electron densities, e.g., in Procyon. For the lines at 76.033 and 78.775 Å the present prediction shows good agreement with the Procyon observation. For the emission line at 91.038 Å, the predicted line intensity ratio at the low densities is lower than the Procyon observation. The contamination from ions with a lower formation temperature becomes non-negligible for the line at 91.038 Å. At high electron densities, the model prediction is in agreement with the solar flare observation, as discussed above. Finally, we note that all the predicted ratios are close to the limit values of low densities (see Table 4).

5. SUMMARY

R-matrix electron-impact excitation data for Fe^{13+} have been calculated using an ICFT approach, in which we include a 197-level close-coupling expansion ($[1s^22s^22p^6]3s^x3p^y3d^z$ ($x+y+z=3$), $3s^24l$ ($l \in s, p, d$, and f), and $3s3p4\{s, p, d\}$) and a larger CI expansion from the additional $3s3p4f$, $3p^24l$, $3p3d4l$, $3d^24l$, $3l4l'4l''$, and $3l3l'5l''$ configurations. The resulting level energies and oscillator strengths were assessed to be reliable by comparison with available experimental data and previous calculations. We compared the results of the present *R*-matrix ICFT calculation with laboratory cross section measurements for the $3s^23p^2\,P^o_{1/2}$–$3s^23p^2\,P^o_{3/2}$ excitation process and with other close-coupling calculations for this and other excitations. These comparisons show that the present results represent an improvement over the previous data of Storey et al. (2000) which is currently used by CHIANTI v6 (Dere et al. 2009).

Using these new data and the present CR model, we have modeled the EUV spectra and compared to solar observations (including SERTS-89, and previous and present *Hinode*/EIS observations). The ratios of line intensities over a short wavelength range are in good agreement between the present model and solar observations, whereas a few line ratios over a longer wavelength range are significantly discrepant.

A series of EUV spectra measured from an EBIT plasma was used to benchmark the solar observation and the present model. The measured ratios are found to be in good agreement with solar observations and theories when contaminations from blending lines are taken into account. Moreover, two weak lines (218.177 Å and 224.354 Å) of Fe XIV were identified and confirmed by the laboratory measurement, which explains a discrepancy previously reported in the electron densities diagnosed from S XII (Keenan et al. 2002). The resulting electron density ($2.3^{+0.8}_{-0.6} \times 10^9$ cm^{-3}) is in good agreement with the previous result ($2.6^{+1.9}_{-1.3} \times 10^9$ cm^{-3}; Storey et al. 2000) for the solar flare on using the updated atomic data.

In the soft X-ray region, the present model has also provided an explanation for another discrepancy, previously reported by Keenan et al. (2006), viz. between the intensity ratio of $\frac{\lambda 70.05}{\lambda 59.40}$ from solar observations and their model's prediction for Fe XV. Also, we point out that the contribution from Fe XIV is limited for a few observed emission lines, e.g., at 70.60 Å in solar flares.

Moreover, two emission lines at 71.34 and 91.01 Å, unknown so far in astrophysical observations, are identified for the first time.

We also note that there is still some unknown and unidentified contamination for several of the emission lines, especially in low-density plasmas as indicated by the Procyon observations. We have shown that systematic laboratory measurements provide a crucial benchmark for theoretical modeling and the clarification of blending problems in observed spectra.

The work of the UK APAP Network is funded by the UK STFC under grant PP/E001254/1 with the University of Strathclyde. G.Y.L. thanks the National Basic Research Program of China (973 Program) under grant 2007CB815103 for travel to, and local support in, Beijing. G.D.Z. acknowledges support from STFC via the Advanced Fellowship program.

REFERENCES

Acton, L. W., Bruner, M. E., Brown, W. A., Fawcett, B. C., Schweizer, W., & Speer, R. J. 1985, ApJ, 291, 865
Badnell, N. R. 1986, J. Phys. B: At. Mol. Opt. Phys., 19, 3827
Badnell, N. R., & Griffin, D. C. 2001, J. Phys. B: At. Mol. Opt. Phys., 34, 681
Beiersdorfer, P., Träbert, E., & Pinnington, E. H. 2003, ApJ, 587, 836
Brenner, G., Crespo López-Urrutia, J. R., Harman, Z., Mokler, P. H., & Ullrich, J. 2007, Phys. Rev. A, 75, 032504
Brickhouse, N. S., Raymond, J. C., & Smith, B. W. 1995, ApJS, 97, 551
Brown, C. M., Feldman, U., Seely, J. F., Korendyke, C. M., & Hara, H. 2008, ApJS, 176, 511
Bryans, P., Landi, E., & Savin, D. W. 2009, ApJ, 691, 1540
Burgess, A. 1974, J. Phys. B: At. Mol. Opt. Phys., 7, L364
Burgess, A., & Tully, J. A. 1992, A&A, 254, 436
Del Zanna, G. 1999, PhD thesis, Univ. of Central Lancashire
Del Zanna, G. 2010, A&A, 514, A41
Del Zanna, G., & Ishikawa, Y. 2009, A&A, 508, 1517
Del Zanna, G., Storey, P. J., & Mason, H. E. 2010, A&A, 514, A40
Dere, K. P., et al. 2009, A&A, 498, 915
Dong, C. Z., Kato, T., Fritzsche, S., & Koike, F. 2006, MNRAS, 369, 1735
Dufton, P. L., & Kingston, A. E. 1991, Phys. Scr., 43, 386
Epp, S. W., et al. 2007, Phys. Rev. Lett., 98, 183001
Froese Fischer, C. 1991, Comput. Phys. Commun., 64, 369
Froese Fischer, C., & Liu, B. 1986, At. Data Nucl. Data Tables, 34, 261
Froese Fischer, C., Tachiev, G., & Irimia, A. 2006, At. Data Nucl. Data Tables, 92, 607
Griffin, D. C., Badnell, N. R., & Pindzola, M. S. 1998, J. Phys. B: At. Mol. Opt. Phys., 31, 3713
Gu, M. F. 2008, Can. J. Phys., 86, 675
Gupta, G. P., & Msezane, A. Z. 2001, J. Phys. B: At. Mol. Opt. Phys., 34, 4217
Heil, T. G., Kirby, K., & Dalgarno, A. 1983, Phys. Rev. A, 27, 2826
Hossain, S., Tayal, S. S., Smith, S. J., Raymond, J. C., & Chutjian, A. 2007, Phys. Rev. A, 75, 022709
Huang, K. N. 1986, At. Data Nucl. Data Tables, 34, 1
Keenan, F. P., Drake, J. J., Chung, S., Brickhouse, N. S., Aggarwal, K. M., Msezane, A. Z., Ryans, R. S. I., & Bloomfield, D. S. 2006, ApJ, 645, 597
Keenan, F. P., Katsiyannis, A. C., Ryans, R. S. I., Reid, R. H. G., Zhang, H. L., Pradhan, A. K., & Widing, K. G. 2002, ApJ, 566, 521
Lang, J., et al. 2006, Appl. Opt., 45, 8689
Lapierre, A., et al. 2007, Rev. Sci. Instrum., 78, 123105
Liang, G. Y., Whiteford, A. D., & Badnell, N. R. 2008, J. Phys. B: At. Mol. Opt. Phys., 41, 235203
Liang, G. Y., & Zhao, G. 2008, MNRAS, 384, 489
Liang, G. Y., et al. 2009a, ApJ, 696, 2273
Liang, G. Y., et al. 2009b, ApJ, 702, 838
Loch, S. D., Pindzola, M. S., Ballance, C. P., & Griffin, D. C. 2006, J. Phys. B: At. Mol. Opt. Phys., 39, 85
Malinovsky, M., & Heroux, L. 1973, ApJ, 181, 1009
Mason, H. E. 1994, At. Data Nucl. Data Tables, 57, 305
Moehs, D., & Church, D. 1999, ApJ, 516, L111
Raassen, A. J. J., et al. 2002, A&A, 389, 228
Smith, S. J., Chutjian, A., & Lozano, J. A. 2005, Phys. Rev. A, 72, 062504
Storey, P. J., Mason, H. E., & Saraph, H. E. 1996, A&A, 309, 677
Storey, P. J., Mason, H. E., & Young, P. R. 2000, A&AS, 141, 285
Summers, H. P. 2004, The ADAS User Manual Version 2.6, http://www.adas.ac.uk/
Summers, H. P., et al. 2006, Plasma Phys. Control. Fusion, 48, 263
Tayal, S. S. 2008, ApJS, 178, 359
Thomas, R. J., & Neupert, W. M. 1994, ApJS, 91, 461
Träbert, E., Heckmann, P. H., Hutton, R., & Martinson, I. 1988, J. Opt. Soc. Am. B, 5, 2173
Träbert, E., Wagner, C., Heckmann, P. H., & Möller, G. 1993, Phys. Scr., 48, 593
Wang, Y.-M., et al. 1997, ApJ, 485, 419
Young, P. R., Landi, E., & Thomas, R. J. 1998, A&A, 329, 291
Young, P. R., Watanabe, T., Hara, H., & Mariska, J. T. 2009, A&A, 495, 587